Chalcogenide Letters

Tech Science Press

http://doi.org/10.32604/cl.2026.084991

ARTICLE

Bandgap Tunable PbSnSeS Quaternary Quantum Dots for near-Infrared Optoelectronic and Solar Cell Applications

M. Irshad Ahamed[1,*], P. J. Suresh Babu[2], R. Lal Raja Singh[3], S. Sivamani[2] and R. Leena Rose[4]

[1]Department of Electronics and Communication Engineering, E.G.S. Pillay Engineering College, Nagapattinam, Tamilnadu, India
[2]Department of Electrical and Electronics Engineering, E.G.S. Pillay Engineering College, Nagapattinam, Tamilnadu, India
[3]Department of Electrical and Electronics Engineering, KIT-Kalaignarkarunanidhi Institute of Technology, Coimbatore, Tamilnadu, India
[4]Department of Electrical and Electronics Engineering, Sri Ranganathar Institute of Engineering and Technology, Coimbatore, Tamilnadu, India
*Corresponding Author: M. Irshad Ahamed. Email: irshad_bcet@yahoo.co.in

Received: 03 May 2026; Accepted: 29 June 2026; Published: 07 August 2026

ABSTRACT: Semiconductor quantum dots (QDs) with tunable narrow bandgaps have emerged as promising materials for next-generation near-infrared (NIR) optoelectronic and photovoltaic devices because their optical properties can be tailored through composition and quantum confinement. Among IV–VI chalcogenide nanomaterials, quaternary alloy systems provide greater compositional flexibility than conventional binary and ternary counterparts; however, PbSnSeS quantum dots remain largely unexplored despite their potential for broadband infrared applications. Here, the structural, electronic, and optical properties of PbSnSeS quaternary QDs synthesized by a one-pot colloidal hot-injection method are systematically investigated. The crystalline IV–VI chalcogenide phase and successful quaternary alloy formation were confirmed by X-ray diffraction (XRD) and energy-dispersive X-ray spectroscopy (EDX), while scanning electron microscopy (SEM) revealed particle sizes in the range of 6–20 nm. The composition- and size-dependent optical behavior was further interpreted using the L.E. Brus model, hyperbolic band model, compositional bandgap estimation, exciton Bohr radius analysis, and density-of-states (DOS) calculations. UV–Vis–NIR spectroscopy exhibited a strong absorption peak at approximately 1675 nm, corresponding to an optical bandgap of 0.74 eV, whereas photoluminescence measurements showed intense NIR emission centered near 1650 nm with a relatively narrow linewidth. The combined theoretical and experimental results demonstrate tunable optical characteristics spanning the visible to near-infrared spectral region. Although lead-containing quantum dots raise environmental concerns, partial substitution of Pb with Sn provides a comparatively lead-reduced alloy while retaining favorable narrow-bandgap optical properties. Overall, the findings identify PbSnSeS quaternary quantum dots as promising candidates for near-infrared optoelectronics, infrared photonics, and next-generation tandem solar cell applications.

KEYWORDS: Quantum dots; chalcogenide; solar cell; optoelectronics

1 Introduction

Increasing power consumption has resulted in a growing demand for energy globally. Solar energy technology has been a focus of long-term renewable energy research. This reliable energy supply and clean environment position it as one of the major technologies. Due to its excellent absorption of sunlight and low cost, solar cells are rapidly becoming a predominant energy source. Successive generations of solar cells have brought considerable progress in efficiency, cost, and technology [1–3]. The International Renewable

Energy Agency (IRENA) has predicted the state of renewable energy until 2050. Solar photovoltaics are predicted to expand most, as shown in Fig. 1.

Since their discovery, solar cells have experienced very impressive progress, where three different generations of solar cell technologies have been developed. The type of first-generation solar cells that dominate the current market is thick wafers formed from single-crystalline or multi-grain silicon or gallium arsenide. Such solar cells can be more efficient than the future generations, but it is a major problem for their preparation still requiring plenty of manual work and being expensive. Second-generation solar cells feature a lower thickness, less materials required, and lower production costs. Cadmium telluride, copper indium gallium selenide, and amorphous silicon are the three primary varieties of second-generation solar cells. Nonetheless, the reduced material consumption, toxicity, and manufacturing processes come at the expense of decreased efficiency [4].

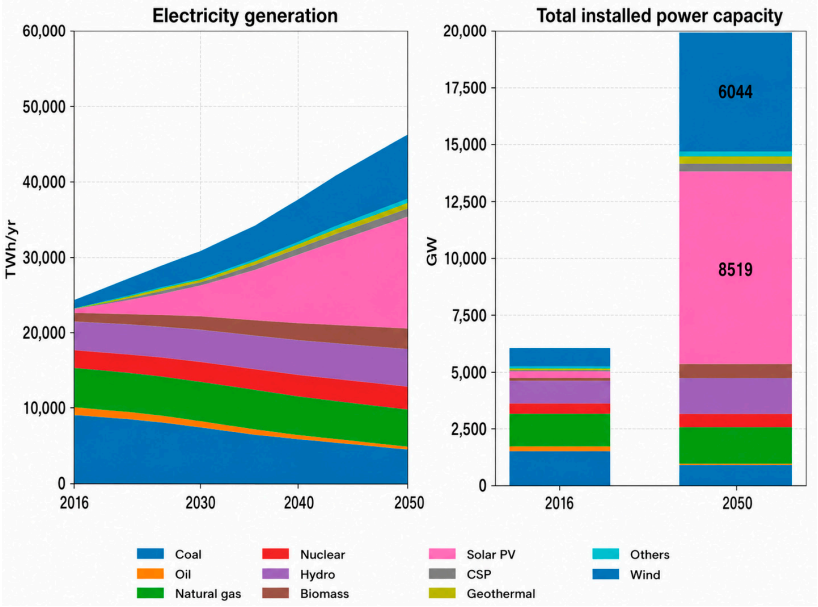

Figure 1: Projected global electricity generation and total installed power capacity by energy source through 2050 [5].

The primary objective of third-generation solar cells is to advance thin-film technology to produce solar cells with high efficiency and cost-effectiveness. Numerous tactics are examined for this purpose. Examples of this phenomenon include quantum-dot, dye-sensitized, and perovskite solar cells. Third-generation solar cells are being made from a variety of new materials besides silicon, including solar inks using conventional printing press technologies, organic dyes, and conductive polymers. First-generation solar cells are the most common type in the market today, because they have superior efficiency and silicon is very abundant on our planet. Second-generation solar cells, meanwhile, account for only about 20% of the market [4].

The optical and electronic properties of quantum dots (QDs) can be manipulated by varying the particle size and composition, making them very attractive for photovoltaic and optoelectronic devices. The absorption and emission properties of QDs are size-dependent and can be manipulated to harvest light efficiently in a wide spectral range due to quantum confinement effects. The attributes of these aforementioned properties render QDs as promising materials for next-generation solar cells, especially in tandem architectures where materials with complementary absorption regions are used to enhance solar energy conversion efficiency [6]. Recent investigations have also targeted increasing the stability and spectral tunability, and scalable fabrication of photovoltaic materials based on QDs. Besides the traditional

colloidal quantum dot solar cells, the ability to tune the absorption properties of QDs and to collect photons in the infrared makes them attractive for use in perovskite photovoltaics and semitransparent solar cells [7,8].

The IV–VI chalcogenide QDs have drawn significant interest where they exhibit high exciton Bohr radius, narrow bandgap, and strong absorption in the near-infrared (NIR) and mid-infrared (MIR) spectral region [9]. The optical and electronic properties of binary lead chalcogenides like PbS, PbSe and PbTe have been found useful for infrared photodetector, thermophotovoltaic device, gas sensor, thermal imaging, and diode lasers [10,11]. Their optical response is tunable by controlling their size down to the nanoscale, allowing absorption/emission over a wide spectral range. Although binary IV–VI quantum dots are excellent infrared emitters, they are not highly compositionally flexible due to the strong lattice parameter dependence of their electronic structure.

The bandgap of ternary alloy systems whose composition varies with bandgap, including $Pb_{1-x}Sn_xTe$, $Pb_{1-x}Sn_xSe$, PbSnS and $PbS_{1-x}Se_x$ has been extensively studied. Optical and electronic properties in these systems can be altered by substituting either cationic or anionic species, an approach also utilized in traditional binary nanocrystals. Nonetheless, due to the possibility of changing only a single sublattice, the degree of band structure engineering and optical tunability is not as high. In comparison, the quaternary PbSnSeS quantum dot system provides a larger compositional space through concomitant cationic (Pb/Sn) and anionic (Se/S) substitution, which allows further versatility in adjusting the electronic structure, carrier confinement, optical transitions, and near-infrared response. Sn incorporation into Pb-based chalcogenides can also partially lower Pb concentration without loss of narrow-bandgap infrared properties, but the incorporation of sulfur into PbSnSe-type systems can affect alloy stability and optical defect-related behavior. Even though binary PbS and PbSe quantum dots and ternary systems (like PbSnSe, PbSnS, and PbSSe) have been widely investigated in the field of infrared optoelectronics, very little work has been done on quaternary PbSnSeS quantum dots [12,13]. Thus, PbSnSeS is one of the intriguing multinary IV-VI alloy systems that can be used to study composition-sensitive optical and electronic properties in near-infrared optoelectronic materials.

Due to the quantum confinement effect, the optical properties of semiconductor nanocrystals change significantly as the particle size decreases, and thus the electronic energy levels and transition energies change. The Brus model, as well as the Hyperbolic Band model, have received wide use for understanding the dependence of the optical bandgap and/or the emission wavelength on the dimensions of the nanoparticles. These theoretical models are useful for understanding the changes in narrow-bandgap semiconductor nanocrystals when they are confined. Furthermore, bandgap estimation and density-of-states (DOS) analysis according to composition could help to understand the effect of alloy composition on the distribution of carriers and optical transitions in quaternary semiconductors.

Lead chalcogenide QDs still show good promise for use in NIR optoelectronic applications; however, several scientific issues are yet to be addressed. Nanomaterials made from lead are known to be toxic, and to ensure the formation of a homogeneous quaternary alloy, the composition must be controlled to prevent the segregation of phases and compositional inhomogeneity [14]. Despite the excellent optical and electronic properties of Pb-based QDs, environmental impacts and toxicity are important issues since lead is a dangerous heavy metal. Uncontrolled discharge of Pb^{2+} ions can lead to environmental pollution and potential biological hazards. However, some studies have shown that under the same degradation conditions, Pb-chalcogenide quantum dots may be less toxic than traditional Cd-based quantum dots because of the higher acute toxicity of the Cd^{2+} ion. Furthermore, part of the Pb can be replaced by Sn in a quaternary alloy system, like PbSnSeS, in which the infrared optoelectronic characteristics can still be

favorable in spite of the lower lead concentration. In addition, encapsulation methods, surface passivation and core-shell structures are extensively investigated to enhance chemical stability and reduce potential leakage of Pb during operation of the devices [15,16]. Thus, PbSnSeS quantum dots may not be regarded as completely benign materials for the environment but rather as comparatively less harmful alternatives to Cd for next generation NIR optoelectronic and photovoltaic applications.

Furthermore, the interplay between simultaneous cation–anion substitution on the optical response and electronic structure of PbSnSeS quantum dots has not been studied in detail. Hence, in the present work, synthesis and optical properties of PbSnSeS quaternary quantum dots were investigated both experimentally and theoretically. The morphology of the particles and their optical properties were investigated using scanning electron microscopy (SEM) and UV–Vis–NIR absorption, photoluminescence (PL) spectroscopy, XRD and EDX respectively. Furthermore, theoretical analysis using Brus Model, Hyperbolic Band Model, composition-dependent bandgap estimation and DOS calculations were used to assess the effect of alloy composition on electronic and optical properties of PbSnSeS QDs.

2 Theoretical Framework

The energy band gap of QDs is influenced by the size dimensions and the effective mass of excited electrons and holes within the material. The mole fraction of Pb is the primary constituent in PbSnSeS QDs, which influences the energy bandgap. The wavelength absorption can be obtained by the relationship of energy gap and wavelength.

2.1 Energy Band Gap Variation of PbSnSeS by Vegard's Interpolation Principles

Since the composition of alloys has a significant effect on the electronic and optical performance of optoelectronic devices, it is important to investigate the variation of energy bandgap in IV–VI semiconductor alloys. In contrast, experimentally reported bandgap data on quaternary alloy systems like PbSnSeS is limited across the entire composition range. Hence, interpolation schemes are frequently used to predict the composition-dependent bandgap from known data on analogous binary and ternary compounds.

Vegard's law is a phenomenological model, whereby the bulk properties can be described by a weighted sum of its constituent compounds. While an ideal Vegard relation describes a linear variation of material properties with composition, actual semiconductor alloys can show small deviations from this behavior due to lattice strain, compositional disorder and band-bowing effects. Nonetheless, for higher-order chalcogenide systems with incomplete experimental datasets, the interpolation approach is a robust first-order prediction tool for bandgap evolution [17,18].

In this work, the energy bandgap of the PbSnSeS quaternary alloy was predicted via weighted contributions from the related ternary alloy subsystems. For the PbSnSeS alloy system, composition variables x and y are cationic and anionic substitution fractions, respectively (where 'x' represents the Pb/Sn ratio, and 'y' for Se/S). The two variables span continuously in the range of 0–1, thus allowing systematic tuning of the electronic and optical properties of the quaternary alloy. The corresponding binary and ternary alloy systems bound the compositional (x, y) space, where certain limiting values of x and y reduce the quaternary composition into its simpler alloy subsystems. The quaternary alloy bandgap was approximated using a weighted linear contribution from the other four related ternary alloy classes: PbSnSe, PbSnS, PbSeS, and SnSeS. The weighting factors $x(1 - \mathrm{x})$ and $y(1 - y)$ represent the compositional mixing contributions from the cationic and anionic sublattices, respectively, in a quaternary alloy structure [19]. Frameworks based on such compositional interpolation are routinely employed to estimate the material parameters of multicomponent semiconductor alloys when experimental data across the entire composition range are

not available. Based on these compositional weighting considerations, the energy bandgap of the PbSnSeS quaternary alloy was calculated using the interpolation relation given in Eq. (1).

$$E_g(x,y) = \frac{x(1-x)[yE_gPbSnSe(x)+(1-y)E_gPbSnS(x)}{x(1-x)+y(1-y)} + \frac{y(1-y)[xE_gPbSeS(y)+(1-x)E_gSnSeS(x)}{x(1-x)+y(1-y)} \quad (1)$$

2.2 Wavelength Analysis by L.E. Brus Model

The energy bandgap of semiconductor QDs exhibits size-dependent behavior due to quantum confinement of charge carriers in nanoscale dimensions. Of these, the Brus model is notably used as one of the prevalent methods to examine how particle size affects bandgap energy. When the particle radius decreases, electrons and holes become more strongly confined, resulting in an increasing bandgap energy.

In the work presented above, the bandgap variation with particle radius was estimated using the Brus model, and for comparison, we show only the simplified expression (adopted herein) given in Eq. (2):

$$E_g(QD) = E_g(bulk) + \frac{h^2}{8R^2\left(\frac{1}{me^*} + \frac{1}{mh^*}\right)} \quad (2)$$

The symbol E_g represents the band gap energy of QDs, while $E_g(bulk)$ denotes the energy band gap of a bulk semiconductor. The variable R corresponds to the radius of the QDs. Additionally, me^* and mh^* represent the effective masses of the electron and hole, respectively. Lastly, 'h' signifies Planck's constant.

The Coulomb interaction term between the confined electron and hole was neglected in the present approximation due to the relatively high dielectric constant of the semiconductor material. Under such conditions, the Coulomb interaction energy becomes comparatively small and contributes only a minor negative correction to the calculated bandgap values. More detailed discussions concerning the Brus model, Coulomb interaction effects and breakdown of effective mass approximation can be found elsewhere [20].

2.3 Hyperbolic Band Model

For narrow-bandgap semiconductors, the conventional effective mass approximation based on parabolic dispersion becomes insufficient because it is valid only near the Brillouin zone center (k ≈ 0). In contrast, the hyperbolic band model provides a more realistic description of non-parabolic energy dispersion and is therefore better suited for Pb-based chalcogenide quantum dots. For systems exhibiting anisotropic electronic properties, this model also offers improved insight into band evolution along different crystallographic directions [21].

Compared with the Brus model, the hyperbolic band model more accurately captures the size-dependent band structure of confined carriers by accounting for deviations from parabolicity. Neglecting Coulomb interaction, the size-dependent bandgap is expressed as:

$$E_g(QD)^2 = {E_g}^2 + \frac{E_g\pi^2 2\hbar^2}{m_0R^2}\frac{1}{2}\left(\frac{1}{me^*} + \frac{1}{mh^*}\right) \quad (3)$$

More detailed discussions concerning the hyperbolic band model, approximation can be found elsewhere [21].

2.4 Variation of Exciton Bohr Radius

The exciton Bohr radius is a key material parameter which provides information on the spatial extension of the excitonic wavefunction in a semiconductor. The confinement strength in semiconductor QDs can

be assessed by the comparison between their size and that of exciton Bohr radius. Two different regimes must be taken into account: strong and weak confinement. Strong confinement can be considered as a situation in which particles or entities are being constrained within a small volume, with hindered mobility or interaction. In the case of weak confinement, the exciton Bohr radius is much smaller than that of semiconductor nanostructure. This means that the QDs is significantly larger than the ordinary exciton length of scale. The exciton Bohr radius remains an important quantity, but its direct impact on the electrical properties of a material may be diminished in the weak confinement case. Other factors are more critical, however, including the size of the nanoparticle. An elementary way, in which the quantum confinement can be observed in a semiconductor, is to reduce the dimensions of the material such that they become less than exciton Bohr radius. Here is the expression for exciton Bohr radius (r_B) that represents bonded electron-hole pair [22]:

$$r_B = \frac{\varepsilon \hbar^2}{e^2}\left(\frac{1}{me^*} + \frac{1}{mh^*}\right) \tag{4}$$

2.5 Density of States

The density of states (DOS) is a key parameter governing the electronic and optical behavior of quantum-confined nanomaterials, as it determines the distribution of available energy levels for charge carriers. In low-dimensional systems, DOS deviates from bulk characteristics, significantly influencing optical absorption and emission properties.

In this study, the DOS for the quantum-confined system is described using the final expression derived in Ref. [23]:

$$D(E) = \frac{1}{l\hbar\pi}\sqrt{\frac{m^*}{2E}} \tag{5}$$

where m^* is the effective mass of the charge carrier, E is the energy, and l is the characteristic confinement dimension. This formulation indicates an inverse square-root dependence of DOS on energy, which contributes to the observed spectral broadening in absorption and photoluminescence measurements of PbSnSeS quantum dots.

3 Synthesis of PbSnSeS QDs

Colloidal hot-injection method was used to synthesize a PbSnSeS quaternary QDs under a nitrogen atmosphere. The cation precursors were lead acetate trihydrate, $Pb(CH_3COO)_2{\cdot}3H_2O$; and tin chloride dihydrate, $SnCl_2{\cdot}2H_2O$; selenium was provided by selenourea and sulfur was provided by thiourea. For the typical synthesis, 1-octadecene (ODE), oleic acid (OA) and oleylamine (OLA) were used as the synthesis medium, and $Pb(OAc)_2{\cdot}3H_2O$ and $SnCl_2{\cdot}2H_2O$ were dispersed under continuous magnetic stirring. The precursor solution was heated to the reaction temperature after degassing for about 30 min at 100°C to remove the water and dissolved oxygen in the precursor solution.

The molar ratio of the precursors used for the synthesis was kept constant at 1:0.5:1:1 (Pb:Sn:Se:S). The selenium–sulfur precursor solution was quickly added to the reaction flask through selenourea and thiourea in OLA, while operating at 180°C under a flow of N2 gas. After injection, the reaction mixture was kept at the same temperature to allow nanocrystal growth and alloying for 15 min. The reaction was then stopped by dropping the temperature of the mixture immediately to room temperature. The synthesized PbSnSeS quantum dots were repeatedly reprecipitated by ethanol/hexane to discard the excess ligand and

remaining precursor species. The purified nanocrystals were then re-dispersed in hexane for additional optical and morphological studies.

Reproducibility was assessed by repeating the synthesis across various batches under the same conditions. The peaks for both the absorption and the photoluminescence bands measured with UV–Vis–NIR instruments were found to be similar for various batches, revealing reproducible optical properties related to the formation of PbSnSeS nanocrystals. It was found that the reaction temperature, precursor concentration and growth time significantly affect the growth behavior of the quantum dots and their optical response.

4 Theoretical Parameters

Table 1 lists the parameters used for calculations.

Table 1: Parameters used in the calculations.

S. No	Parameters	Values	Literature
1	$PbSnS_3$ Energy gap	1.68 eV	[24]
2	PbSnSe Energy gap	0.2 eV	[25,26]
3	SnSSe Energy gap	1.7 eV	[27]
4	PbSSe Energy gap	1.0 eV	[28]
5	Effective mass of electron and hole in SnSe	0.41 mo and 0.48 mo	[29,30]
6	Effective mass of electron and hole in SnS	0.35 mo and 0.55 mo	[29]
7	Effective mass of electron and hole in PbSe	0.084 mo and 0.070 mo	[31]
8	Effective mass of electron and hole in PbS	0.12 mo and 0.11 mo	[31]
9	High frequency dielectric constant	~13.1	[32]

5 Results and Discussion

5.1 UV-Vis-NIR Spectrum

The UV–Vis–NIR absorption spectrum of PbSnSeS QDs (Fig. 2) demonstrates unique and characteristic optical properties arising from quantum confinement effects as well as alloying effects in these multinary chalcogenide systems (PbSnSeS). The maximum absorbance is at approximately 1675 nm, and broader range between about 600 and 1800 nm shows well-defined sharp peak indicating a strong excitonic dipolar interaction in the NIR.

In particular, the NIR peak has been attributed to highly direct low bandgap transition—singular for QDs. By entering the NIR, the profile of the absorption tail sharpens (which indicates intermediate energy states and more complex band structure). PbSnSeS QDs, the cooperative interaction of several cation (Pb^{2+}, Sn^{2+}) and anion (Se^{2-}, S^{2-}) elements provides attractive flexibility to adjust bandgap through the hybridization effect of s–p orbitals, leading to broad absorption coverage in the visible to NIR region. The absorption peak is strongly red-shifted compared to the phase-pure PbS/SnS quantum dots. This indicates that a homogeneous PbSnSeS alloy was indeed obtained. The alloy causes a synergistic reduction of the bandgap evidenced by absorbing strongly even in NIR with an excitonic feature centered at 1675 nm. The optical bandgap ~0.74 eV was estimated from the experimentally observed near-infrared absorption peak centered at approximately 1675 nm using the photon energy wavelength relationship $Eg = hc/\lambda$ which is in good agreement with the reported fitting results. The peak intensity and the monodispersivity in NIR confirm the successful formation of size-narrowed QDs and a homogeneous alloy composition, resulting from efficient synthesis and high ligand stabilization. These peak properties indicate that PbSnSeS quantum dots are promising candidates for the wide-bandwidth absorption of infrared photodetectors, low bandgap solar cells as well as QD lasers.

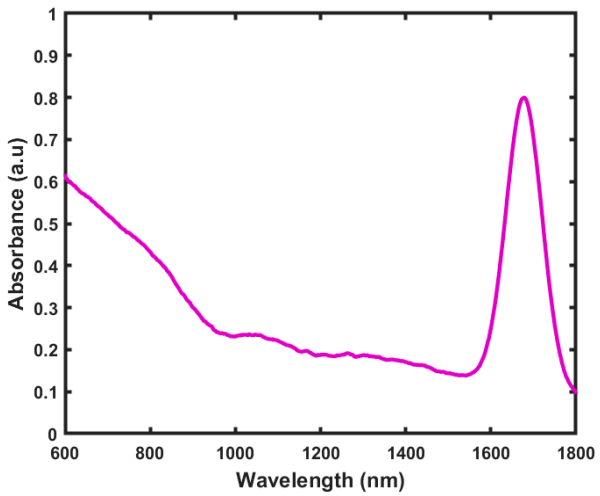

Figure 2: UV-Vis-NIR spectrum of PbSnSeS QDs.

5.2 Photoluminescence Spectra

The PL spectrum of the PbSnSeS QDs in Fig. 3 displays a strong Near-Infra-Red (NIR) emission peak at about 1650 nm, which corresponds to the efficient radiative recombination of the photogenerated excitons in the quaternary nanocrystal system. The sharp, strong emission feature reveals excellent crystalline quality, and stability of the optical response of the synthesized quantum dots. The emission characteristics were quantified by fitting the PL profile with a Gaussian function, which had a very good fitting with experimental PL spectrum with a goodness of fit $R^2 \approx 0.995$. The fitted spectrum yielded a full width at half maximum (FWHM) of about 80 nm. The relatively small linewidth suggests good uniformity of the optical emission with less defect-assisted recombination and better compositional homogeneity in the PbSnSeS alloy structure.

The broad baseline emission extending from nearly 1000 to 1800 nm can be attributed to particle size distribution, compositional variation, and possible phonon-assisted recombination processes. The linewidth broadening is also in agreement with the SEM analysis which showed nanocrystal sizes of 6–20 nm. The contribution of smaller particles is dominant for the optical transitions related to the confinement while the contribution of the relatively larger particles is dominant for the broadening of the spectrum and the slight red shift in the near infrared region. The PL peak position is in good agreement with the absorption features observed in UV–Vis–NIR spectrum, which supports the quantum-confined optical behavior of the PbSnSeS QDs and indicates that the PbSnSeS has a tunable direct bandgap close to 0.76 eV. The small difference between the absorption and emission peaks can be attributed to excitonic relaxation and carrier cooling processes found in semiconductor quantum dots.

The high absorption properties around the band edge region further confirm the efficient interaction between photons and the PbSnSeS quantum dots. The optical absorption coefficient of the quaternary nanocrystal system is estimated to be 10^5 cm^{-1}, typical of highly absorbing lead-chalcogenide semiconductor nanomaterials. With such a large absorption coefficient, efficient light harvesting is possible using relatively thin active layers, allowing the use of PbSnSeS QDs in infrared photonic applications such as infrared photodetection, NIR optoelectronic devices, and broadband photovoltaic systems.

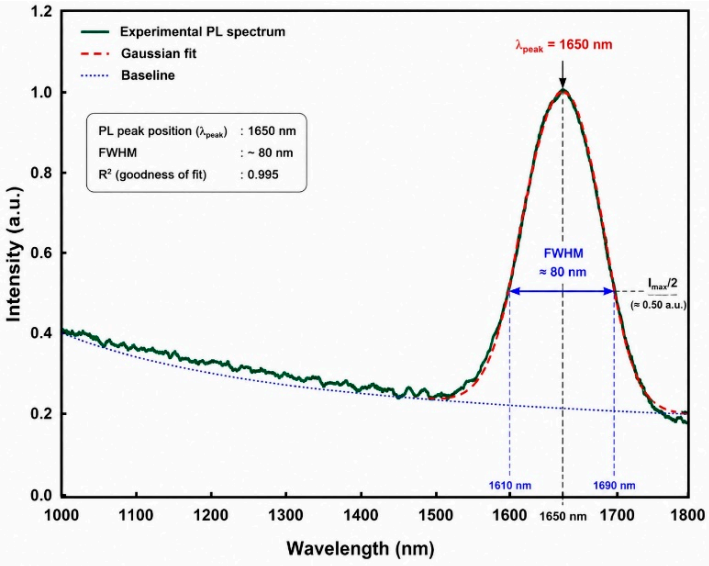

Figure 3: PL Spectra of PbSnSeS QDs.

It has been demonstrated in previous studies of PbS-, PbSe-, and related alloyed lead-chalcogenide QDs that both the photoluminescence quantum yield (PLQY) and radiative efficiency (RE) are sensitive to surface passivation, compositional tuning, and defect-assisted recombination effects [33,34]. The PLQY of a lead-chalcogenide QD has been estimated quantitatively through absolute measurement using an integrating sphere or a comparative method using a calibrated reference standard, integrated emission intensity analysis, and absorbance correction at the excitation wavelength. While no quantitative PLQY analysis was carried out in the current study, the observed PL response at the near infrared region suggests that the synthesized nanocrystals exhibit radiative emission behavior. The emission features obtained in the NIR-II/SWIR spectral window are indicative of potential applications for the PbSnSeS quantum dots in infrared optoelectronics and wavelength selective photonics. Calibrated photoluminescence quantum yield, integrating-sphere-based analysis, time-resolved photoluminescence studies are planned for future work to gain deeper insight into carrier recombination dynamics and optoelectronic efficiency of the synthesized quaternary nanocrystals.

5.3 SEM Analysis

The surface morphology and structural nature of the synthesized PbSnSeS quantum dots were investigated using SEM as shown in Fig. 4. The micrograph, taken at 100.0 kx magnification and 15.0 kV accelerating voltage, shows a distinctly uniform distribution of granular morphology, which is composed of discretely dispersed nanocrystallites that are loosely packed. The overall average size of the nanocrystals was found to be in the 6–20 nm range, indicating their quantum-confinement nature as derived from the alloyed Pb–Sn–Se–S system.

The HRSEM image reveals the nanoparticles as spherical to polyhedral shapes dispersed with negligible aggregation, resulting from the effective encapsulation by dispersing ligands oleic acid and oleylamine during the process. The particle distribution in the film is highly uniform, forming a continuous and smooth film-like structure. The fine particle size and closely packed nature of the QDs are due to controlled growth through optimized one-pot colloidal route. The regular distribution of small-sized individual particles is due to the selected inert N2 atmosphere and stoichiometric balance of metal-chalcogen precursors that immensely inhibited the formation of secondary phases, thus promoting a single-phase solid solution

chalcohalide. Furthermore, absence of large grain clusters or microdefects ensures high colloidal stability and better capping phenomena, which ensures that the optical properties remain reproducible for subsequent electronic processes in the quantum-confined nanomaterials used in the device. From the above, SEM characterization indicates that the PbSnSeS quantum dots have a uniform morphology with good particle distribution and are highly smooth, thus confirming their structural integrity. These findings align well with the optical characterization trend, which exhibits a sharp peak due to excitons, thereby showing a compositionally monodisperse QD system.

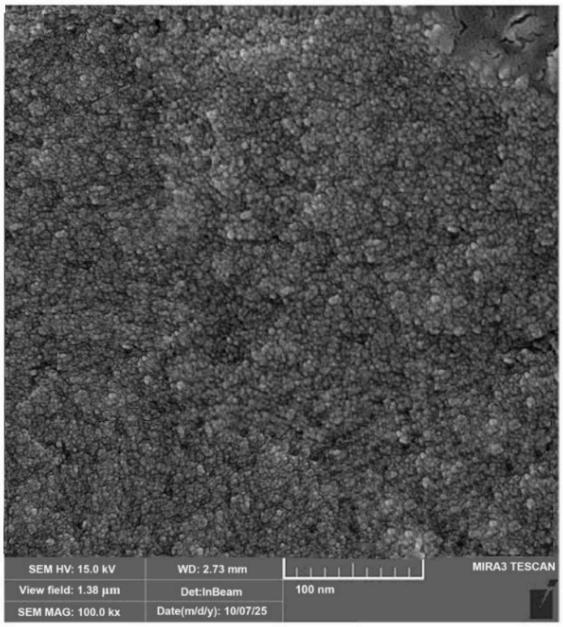

Figure 4: SEM image of PbSnSeS QDs.

SEM analysis revealed that the particle sizes ranged from 6 to 20 nm; however, the optical response is due to the collective response of quantum dots with various sizes and confinement properties. The near-infrared spectrum shows a slight spectral broadening and red shift that are attributed to the relatively larger-sized particles, while the smaller nanocrystals are responsible for the optical transitions due to the confinement. Thus, the experimentally determined measured size distribution compares well with the broadened absorption and photoluminescence spectra. The overall bandgap variation with confinement was primarily explained by the theoretical models described in this work for the smaller quantum-confined PbSnSeS nanocrystals.

5.4 Energy Dispersive X-Ray (EDX) Spectroscopy Analysis

Energy Dispersive X-ray (EDX) spectroscopy analyzed the elemental composition and chemical distribution in the synthesized PbSnSeS quantum dots as shown in Fig. 5. The characteristic peaks of Pb, Sn, Se, and S were obtained from the EDX spectrum, showing the presence of all constituent species associated with the PbSnSeS quaternary alloy system. The lack of noticeable impurity-related peaks within the detection limit of the instrument indicates that the synthesized nanostructures are mostly in the desired multicomponent chalcogenide composition.

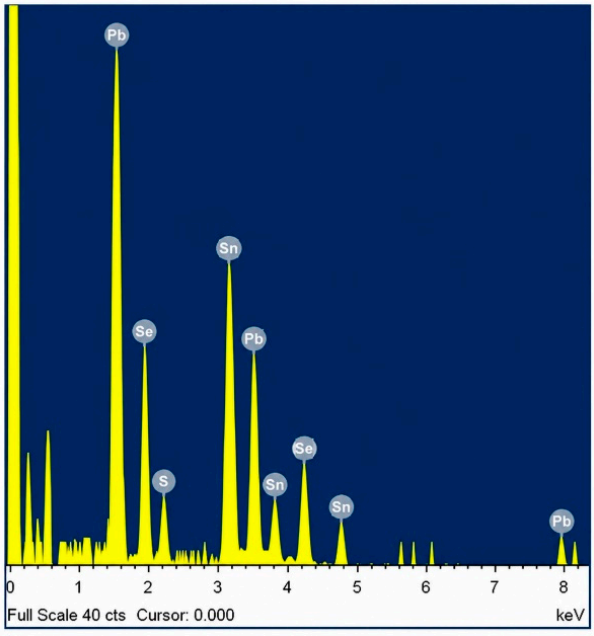

Figure 5: EDX spectrum.

The strong X-ray scattering intensity of lead, with its high atomic number, explains why the peaks of lead are dominant in the spectrum, while the comparatively lower intensity of the peaks of Sn and S is due to their lower atomic masses and relative concentrations. The presence of both cationic species (Pb and Sn) and anionic species (Se and S) suggests the successful incorporation of multiple elemental components in the synthesized nanocrystals. Such incorporation is significant for achieving band structure modulation through alloy mediation and near-infrared optical tunability of PbSnSeS quantum dots.

The results of the EDX analysis are displayed in Table 2, which shows the estimated elemental composition. The elemental composition values listed in Table 2 show that the main constituent of the synthesized nanocrystals is Pb whereas Sn is present as the second cationic component in the quaternary alloy structure. Simultaneous anionic substitution is confirmed in the PbSnSeS system by the presence of both Se and S. The relatively higher atomic percentage of sulfur is due to its lower atomic mass compared to Pb and Se, while the higher weight percentage of Pb is attributed to its higher atomic mass. The elemental distribution observed is in good agreement with the precursor composition used in synthesis and confirms the formation of a multicomponent PbSnSeS alloy nanostructure. The slight discrepancies between the precursor ratio and the composition determined by EDX analysis may be due to the reactivity difference of the precursors, the alloy incorporation rate, and the semi-quantitative characteristic of the EDX analysis. In general, EDX results yielded the compositional evidence in favor of the formation of quaternary nanostructures of PbSnSeS for further optical and electronic characterization.

Table 2: Elemental composition analysis of PbSnSeS quantum dots obtained from EDX spectroscopy.

Element	Weight (%)	Atomic (%)
Pb	42.18	20.46
Sn	14.37	11.82
Se	25.64	31.25
S	17.81	36.47
Total	100.00	100.00

5.5 XRD Analysis

Fig. 6 shows the X-ray diffraction pattern of the synthesized PbSnSeS QDs, exhibiting sharp diffraction peaks at about 25°, 30°, 42°, 50°, 53°, 61° and 68° corresponding to (111), (200), (220), (311), (222), (400) and (420) crystallographic planes, respectively. The presence of these reflections suggests the creation of a crystal structure of IV-VI chalcogenide alloys in the quaternary system of PbSnSeS. The diffraction behavior was similar to that reported in the literature for Pb-based chalcogenide nanocrystals and the presence of multiple reflections indicates that both cationic (Pb/Sn) and anionic (Se/S) components were incorporated into the lattice successfully.

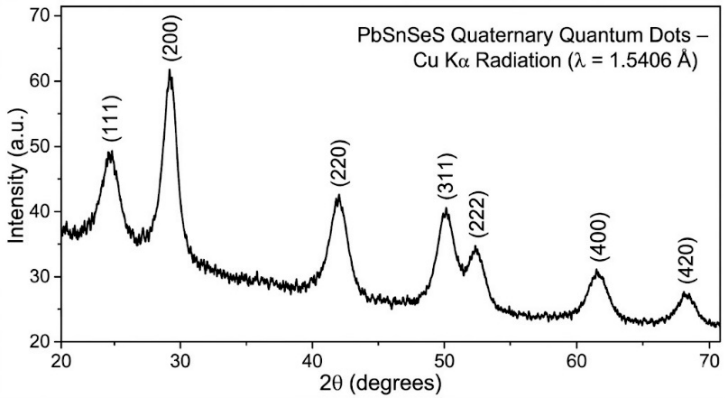

Figure 6: XRD pattern.

The diffraction peaks show significant peak broadening, typical of the formation of nanoscale crystalline domains, and in accordance with the synthesized material being a quantum-dot material. It can be correlated with a the decrease in crystallite size and also be due to local lattice distortion caused by simultaneous alloying of Pb, Sn, Se, and S in the crystal lattice that results in broadening of the diffraction peaks. This is expected due to the small changes in diffraction response from conventional binary PbS and PbSe quantum dots caused by compositional tuning and modification of local bonding environments introduced by substituting Sn for Pb in the sublattice and introducing S into the lattice sites of Se.

The preferred structural ordering in the quaternary nanocrystal system is indicated by the dominant reflection at 30°, corresponding to the (200) plane, while the relatively wide reflections at higher angles are due to the effects of nanoscale confinement and alloy-induced strains. In multinary lead-chalcogenide or alloyed semiconductor quantum dots, both the cationic and anionic substitutions alter the lattice parameter, and the overall crystallographic response to the substitution presents a similar diffraction behavior [35].

The ordering of the lattice structure, the composition of the alloy, both of which are strongly related to the diffraction profile, play an important role in the optical properties of the PbSnSeS quantum dots, as a very close bond between the ordered lattice and the electronic structure of narrow-bandgap chalcogenide systems establishes. The structural features are thus in agreement with the observed near infrared optical response of PbSnSeS quantum dots and are consistent with their being suitable for infrared optoelectronic and photovoltaic applications.

5.6 Energy Bandgap Variation

The energy bandgap of the quaternary alloy is determined by its composition and size-dependent properties, which are analyzed with respect to a general compositional characteristic. The derivation of this parameter is based on a linear correlation between the compositions of groups IV (x) and VI (y) that are

necessary for achieving minimum lattice match. Eq. (1) expresses the energy bandgap change of PbSnSeS by utilizing MATLAB software.

The primary focus of our investigation is to examine the potential energy bandgap of PbSnSeS QDs by varying the mole fraction of Pb. This phenomenon is evident from the information shown in Fig. 7. The energy bandgap can be adjusted within the range of 0.99 eV to 0.64 eV by incrementing x from 0.1 to 1.0 with a step size of 0.05. An increase in the mole fraction of Pb is expected to result in a drop in the energy bandgap of PbSnSeS. This can be attributed to the smaller energy bandgaps of PbS and SnSe.

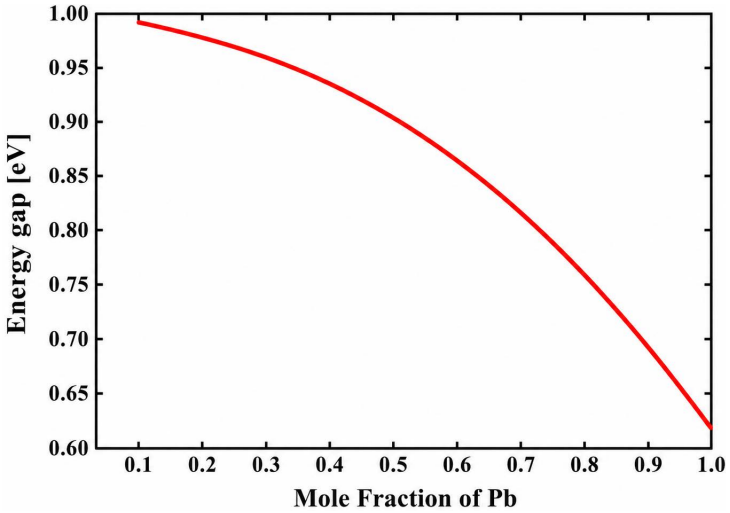

Figure 7: Mole fraction vs. energy bandgap.

A plausible interpretation of the observed variation in Eg, as inferred from the theoretical findings, might be attributed to the increased contribution of Pb in the compound, likely impacting the overall distribution of the electronic structure within the semiconductor nanocrystal. The wavelength of energy conversion devices corresponds to the energy bandgap of the material. As a result, new applications are emerging for PbSnSeS-based optoelectronic devices such as sensors and solar cells.

5.7 Exciton Bohr Radius Variation

Variations in the mole proportion of Pb result in varied values for the compound's exciton Bohr radius. The results showed that when the exciton Bohr radius declined, so did the mole percentage of Pb. Fig. 8 demonstrates that for lower mole fractions of X equal to 0.1, the predicted exciton Bohr radius is 0.35 nm. The computed exciton Bohr radius is 0.04 nm when X equals 1.0. It should be emphasised that the particle size in bulk materials is substantially bigger than the exciton Bohr radius, resulting in continuous bands of energy rather than discrete energy levels. As a result, when compared to QD materials, bulk materials have a substantially narrower band gap between the conduction and valence bands.

The exciton Bohr radius values were estimated using the effective mass approximation together with the dielectric constant parameters listed in Table 1, while the quantum dot dimensions were obtained from SEM analysis. The calculated exciton Bohr radius values (0.04–0.35 nm) are smaller than the observed particle sizes (6–20 nm), indicating that the synthesized PbSnSeS nanocrystals predominantly fall within the weak confinement regime. Under such conditions, the optical response is expected to arise from a combination of confinement-related effects and bulk-like electronic contributions. It should be noted that the calculated Bohr radius is sensitive to the dielectric constant and carrier effective mass values employed

in the model. Since experimentally established intrinsic parameters for the quaternary PbSnSeS system are currently unavailable, the calculations used composition-dependent values derived from reported literature data of related chalcogenide materials. Therefore, the obtained Bohr radius values are intended to represent the relative confinement behavior within the PbSnSeS alloy system rather than absolute values directly comparable to conventional binary Pb-chalcogenide semiconductors.

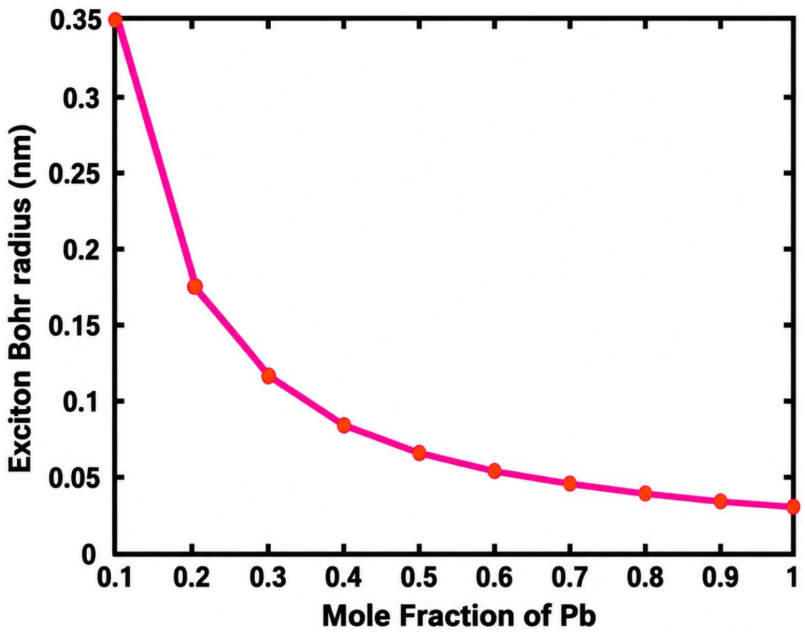

Figure 8: Mole fraction vs. exciton Bohr radius.

5.8 Size Dependent Emission Wavelength in QDs

The size of QDs, which is often characterized by their radius, significantly impacts their optical properties. The relationship between the radius of a QD and its wavelength is one of the fundamental aspects of QD optical properties. QDs vary in size and their energy band structure, resulting in variations in absorption and emission wavelengths. Charge carriers are confined in a small volume, resulting in discrete energies due to the quantum confinement effect. This ability to tune PbSnSeS QDs' size allows them to control absorption and emission wavelengths, making them useful in several applications, such as light-emitting diodes (LEDs), solar cells, and QD displays.

The utilization of PbSnSeS QDs, with their distinctive characteristics, have the potential to significantly enhance the light-to-energy conversion efficiency of solar cells when utilized as a coating material. The nanoscale semiconductor materials can adjust their bandgaps, enabling effective light absorption and the creation of electron-hole pairs. The integration of PbSnSeS QDs into solar cells serves as a means to enhance light absorption capabilities, thereby broadening the absorption spectrum. Moreover, the size-dependent features of these materials provide a more precise alignment with the solar spectrum, resulting in enhanced capture of photons. The effective separation and transmission of charges in QDs significantly augment the overall performance of solar cells, hence positioning them as a potential technology for advancing renewable energy systems.

The spectra for different QDs sizes are shown in Fig. 9, comparing two models: Brus and the hyperbolic band model. When the QD radius is 1 nm, the wavelengths are 341 nm (3.63 eV) and 580 nm (2.13 eV) for the Brus and hyperbolic models, respectively. As the QD radius increases to 3 nm, both models converge to

a wavelength around 1240 nm. When the radius further increases from 4 to 10 nm, the plots for both models diverge significantly, with the compound's wavelength covering the majority of the infrared spectrum. This insight highlights the impact on the solar cell energy conversion process and its role in enhancing electron-hole pair generation. The experimentally observed absorption peak (marked with a triangle symbol) aligns closely with the theoretically predicted wavelength trends derived from both the Brus and hyperbolic band models, thereby validating the quantum confinement-driven tunability of PbSnSeS QDs.

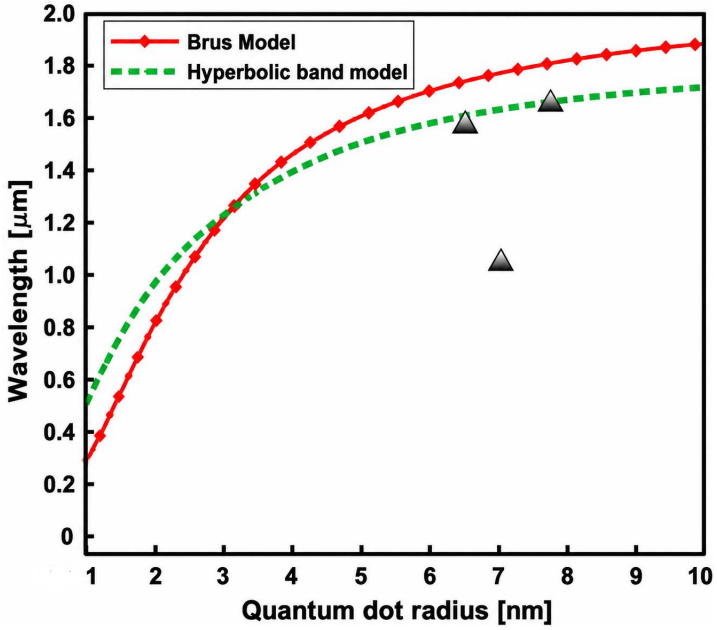

Figure 9: Comparison of wavelength vs. radius for PbSnSeS QDs.

This strong correlation between experimental and theoretical results confirms that as the QD radius decreases, the confinement of charge carriers becomes more pronounced, leading to a blue shift in absorption due to the increased bandgap energy. Conversely, as the QD radius increases, the red shift of the absorption edge toward the infrared region becomes evident, effectively broadening the active spectral range. Such tunability is crucial for solar cell applications, as it allows optimized absorption across the visible to NIR regions of the solar spectrum.

The presence of a sharp, intense absorption band at 1675 nm also signifies efficient alloy-induced band alignment within the PbSnSeS lattice, which promotes enhanced photon capture and improved exciton dissociation efficiency. This behavior demonstrates that the PbSnSeS QDs can serve as highly responsive NIR absorbers, capable of harnessing longer-wavelength photons that conventional semiconductors typically overlook. The smooth and slightly broadened baseline in the UV–Vis–NIR spectrum further indicates a uniform size distribution of QDs with minimal surface defects, supporting stable optical response characteristics.

Overall, the agreement between the experimental data (triangle markers) and theoretical models (Brus and hyperbolic band models) not only validates the formation of high-quality PbSnSeS QDs but also underscores their potential as efficient broadband sensitizers for next-generation solar energy conversion systems. The combination of size-dependent bandgap modulation and extended infrared response makes these nanocrystals promising candidates for use in tandem and multi-junction solar cell architectures, enabling more efficient utilization of the solar spectrum and improved photoelectric conversion efficiency.

5.9 Density of Electronic States as a Function of PbSnSeS Energy

At the nanocrystals' size scale of the excitonic length, quantum confinement effects result in significant changes in the electronic structure. However, due to the spatial confinement of charge carriers in PbSnSeS quantum dots, the energy distribution near the band edges is modified and discrete or quasi-discrete electronic states are formed instead of the continuum of states found in bulk semiconductors. The aforementioned changes may affect the optical absorption properties, excitonic recombination, and carrier transitions in nanoscale chalcogenide systems.

The variation in the density of states (DOS) as a function of energy in the PbSnSeS quantum dots is plotted in Fig. 8. The DOS calculation is based on the effective mass approximation by taking the confined electronic states near the edge of the conduction and valence bands of the quaternary alloy system. It is assumed that the energy dispersion is parabolic, the effective masses of the carriers are isotropic, and the confinement takes place in a characteristic nanoscale dimension. The energy dependence of the available electronic states was described by a reduced dimensional quantum-confined DOS expression as as in Eq. (5). The DOS profiles shown in the Fig. 10 were calculated numerically from Eq. (5) over the energy range of interest with material parameters from the literature, as summarized in the Table 1.

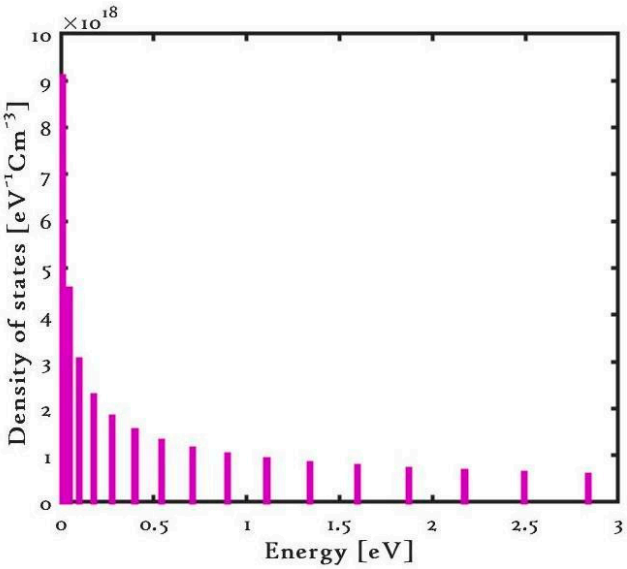

Figure 10: DOS vs. function of energy.

The resulting DOS profile shows an inverse square root energy dependence with the assumed quantum confined model. The energy-dependent density of states (DOS) reveals a relatively higher number of states in the low-energy region, which could potentially affect the transition of carriers and the optical response of the PbSnSeS quantum dot system. This behavior is a result of the redistribution of electronic states as predicted by the theoretical model, which is dependent on the confinement. It is important to note that the present DOS analysis is computational and aimed to bring qualitative understanding of the electronic behavior of the PbSnSeS QDs and not to measure the electronic state density directly.

5.10 Comparison of PbSnSeS QDs with Previous Studies

Table 3 compares the optical characteristics of the proposed PbSnSeS quantum dots with previously reported Pb-based and alloyed IV–VI QD systems for near-infrared applications. Compared with con-

ventional PbS, PbSe, and related alloyed quantum dots, the PbSnSeS system demonstrates strong NIR absorption, relatively narrow emission linewidth, and additional compositional tunability through simultaneous cationic and anionic alloying. These characteristics indicate the potential of PbSnSeS QDs for future infrared optoelectronic and tandem photovoltaic applications.

Table 3: Comparison of PbSnSeS QDs with reported IV–VI quantum dot systems.

Material System	Peak Wavelength (nm)	Absorption Coefficient	FWHM (nm)	Bandgap (eV)	Distinct Features of PbSnSeS System	Reference
PbSnSeS QDs	**~1675–1680**	**10^5 cm^{-1}**	**~80**	**0.74–0.76**	**Strong NIR-II absorption, relatively narrow emission linewidth, compositional bandgap tuning through dual alloying**	**Present Work**
PbS QDs	~1100–2600	10^4 cm^{-1}–10^5 cm^{-1}	>100–150	0.41–1.1	PbSnSeS exhibits narrower spectral linewidth near 1650 nm and additional alloy-assisted tunability	[36,37]
PbSe QDs	~1200–4500	10^4 cm^{-1}	~120–200	0.27–0.9	PbSnSeS demonstrates strong absorption response together with sulfur-assisted compositional tuning	[38,39]
PbSSe Alloy QDs	~1000–1400	10^4 cm^{-1}	~90–110	~0.8–1.2	PbSnSeS extends optical response deeper into the NIR-II region	[20]
PbSnSe Alloy QDs	~1500–2900	Not reported	Not reported	~0.3–0.8	Sulfur incorporation in PbSnSeS may contribute to enhanced optical confinement and band structure modulation	[40,41]
Sn-based Chalcogenide QDs	~800–1200	10^4 cm^{-1}	~150	1.0–1.6	PbSnSeS exhibits a narrower bandgap and stronger NIR absorption characteristics	[42,43]

The near-infrared absorption and photoluminescence spectra of the synthesized PbSnSeS QDs show their potential for infrared optoelectronic and photovoltaic applications. The narrow band gap (~0.75 eV) and NIR-II/SWIR spectral response are favorable for extended infrared light harvesting compared to conventional absorbers in the visible light region. Further, the simultaneous cationic (Pb/Sn) and anionic (Se/S) substitution offers greater compositional flexibility to tune the optical response compared to the binary systems of PbS and PbSe. These properties point to the potential applications of PbSnSeS QDs as an

absorber in future infrared photodetection and tandem PV cells. Further investigations are planned at the device level to assess their actual PV performance at operating conditions.

6 Conclusion

PbSnSeS QDs were successfully synthesized using a one-pot colloidal hot-injection approach and theoretically and experimentally studied. The XRD results confirmed the crystalline IV–VI chalcogenide nature of the nanostructures, and the EDX results justified the incorporation of the elements Pb, Sn, Se, and S, which supported the formation of the quaternary alloy. SEM showed that the particles have a size range of 6–20 nm. The optical characterisation demonstrated the presence of a strong absorption peak in the UV–Vis–NIR region of the spectrum around 1675 nm corresponding to a band gap of the order of 0.74 eV, while the PL measurements revealed intense NIR emission around 1650 nm with a relatively narrow linewidth. Theoretical analysis using the Brus model, hyperbolic band model, compositional bandgap estimation, exciton Bohr radius, and density-of-states (DOS) calculations was done to support the observed composition- and size-dependent optical behavior of the PbSnSeS system. The optical response in the visible–NIR range of the combined results shows tunability attributed to the combination of quantum confinement and alloying effects. While there are still concerns about the environment with respect to lead-based quantum dots, the substitution of a portion of Pb by Sn offers a relatively lead-reduced alternative that still has favorable NIR optical properties. These results indicate that PbSnSeS QDs can be excellent materials for IR optoelectronic devices, photonic devices, and future tandem solar cells. The potential for their practical application will be further evidenced by advanced compositional analysis, quantitative PL efficiency measurements, and device-level validation.

Acknowledgement: Not applicable.

Funding Statement: The authors received no specific funding for this study.

Author Contributions: M. Irshad Ahamed: Conceptualization, methodology, formal analysis, manuscript writing. P. J. Suresh Babu: Supervision, review, and editing. R. Lal Raja Singh: Data curation, language editing. S. Sivamani: Investigation, formal analysis, visualization. R. Leena Rose: Validation, review, and editing. All authors reviewed and approved the final version of the manuscript.

Availability of Data and Materials: The authors confirm that the data supporting the findings of this study are available within the article. Additional data are available from the corresponding author upon reasonable request.

Ethics Approval: Not applicable. This study did not involve human participants, human tissue, animals, or clinical data.

Conflicts of Interest: The authors declare no conflicts of interest.

References

1. Kumar JCR, Majid MA. Renewable energy for sustainable development in India: current status, future prospects, challenges, employment, and investment opportunities. Energy Sustain Soc. 2020;10(1):2. [CrossRef].
2. Gielen D, Boshell F, Saygin D, Bazilian MD, Wagner N, Gorini R. The role of renewable energy in the global energy transformation. Energy Strategy Rev. 2019;24:38–50. [CrossRef].
3. Dada M, Popoola P. Recent advances in solar photovoltaic materials and systems for energy storage applications: a review. Beni Suef Univ J Basic Appl Sci. 2023;12(1):66. [CrossRef].
4. Zhang T, Wang M, Yang H. A review of the energy performance and life-cycle assessment of building-integrated photovoltaic (BIPV) systems. Energies. 2018;11(11):3157. [CrossRef].

5. Rozon F, McGregor C, Owen M. Long-term forecasting framework for renewable energy technologies' installed capacity and costs for 2050. Energies. 2023;16(19):6874. [CrossRef].
6. Babu PJS, Padmanabhan TS, Ahamed MI, Sivaranjani A. Studies on copper indium selenide/Zinc sulphide semiconductor quantum dots for solar cell applications. Chalcogenide Lett. 2021;18(11):701–15. [CrossRef].
7. Shin D, Park Y, Jeong H, Tran HV, Jang E, Jeong S. Exploring the potential of colloidal quantum dots for near-infrared to short-wavelength infrared applications. Adv Energy Mater. 2025;15(2):2304550. [CrossRef].
8. Habiba U, Khan MU, Sultan N, Saeed Ashraf Janjua MR. Next-generation quantum dot solar cells: advances in materials, device engineering and performance optimization. RSC Adv. 2026;16(33):30448–76. [CrossRef].
9. Yarema M, Yazdani N, Yarema O, Đorđević N, Lin WMM, Bozyigit D, et al. Structural ordering in ultrasmall multicomponent chalcogenides: the case of quaternary Cu-Zn-In-Se nanocrystals. Adv Mater. 2024;36(44):2406351. [CrossRef].
10. Sohrabikia Z, Abedi Ravan B, Jafari M. Tuning band gaps in lead chalcogenides under pressure: implications for infrared detection applications. Phys Scr. 2024;99(7):075975. [CrossRef].
11. Ikeri HI, Harry ST, Achuka EI, C N E, Asielue OK, Ndubueze ND. Optical properties of PbSe, PbS, and PbTe semiconductor quantum dots and their applications. Int J Mater Sci Eng. 2024;10(2):19–23. [CrossRef].
12. Sashchiuk A, Yanover D, Rubin-Brusilovski A, Maikov GI, Čapek RK, Vaxenburg R, et al. Tuning of electronic properties in IV–VI colloidal nanostructures by alloy composition and architecture. Nanoscale. 2013;5(17):7724. [CrossRef].
13. Kumar S, Majeed Khan MA, Zulfequar M, Husain M. Optical, structural and electrical investigations on $PbTe_{1-x}Sx$alloys. J Mater Sci. 2007;42(1):363–7. [CrossRef].
14. Huang CY, Li H, Wu Y, Lin CH, Guan X, Hu L, et al. Inorganic halide perovskite quantum dots: a versatile nanomaterial platform for electronic applications. Nanomicro Lett. 2022;15(1):16. [CrossRef].
15. Wang M, Wang W, Ma B, Shen W, Liu L, Cao K, et al. Lead-free perovskite materials for solar cells. Nano Micro Lett. 2021;13(1):62. [CrossRef].
16. Wu P, Zhang F. Recent advances in lead chemisorption for perovskite solar cells. Trans Tianjin Univ. 2022;28(5):341–57. [CrossRef].
17. Woods-Robinson R, Han Y, Zhang H, Ablekim T, Khan I, Persson KA, et al. Wide band gap chalcogenide semiconductors. Chem Rev. 2020;120(9):4007–55. [CrossRef].
18. Schnohr CS. Compound semiconductor alloys: from atomic-scale structure to bandgap bowing. Appl Phys Rev. 2015;2(3):031304. [CrossRef].
19. Guden R, Piprek J. Material parameters of quaternary III–V semiconductors for multilayer mirrors at 1:55 μm wavelength. Model Simul Mater Sci Eng. 1996;4:349. [CrossRef].
20. Ahamed MI, Kumar KS, Anand EE, Sivaranjani A. Optical attenuation modelling of $PbSe_xS_{1-x}$ quantum dots with vegard's law and brus equation use. J Ovonic Res. 2020;16(4):245–52. [CrossRef].
21. Ahamed I, Ahamed M, Kumar KS, Sivaranjani A. Comparative energy bandgap analysis of zinc and tin based chalcogenide quantum dots. Rev Mex De Fis. 2022;68(4):041601. [CrossRef].
22. Ahamed MI, Kumar KS. Modelling of electronic and optical properties of Cu_2SnS_3 quantum dots for optoelectronics applications. Mater Sci Pol. 2019;37(1):108–15. [CrossRef].
23. Ahamed MI, Ahamed M, Muthaiyan R. Modelling of density of states and energy level of chalcogenide quantum dots. Int Rev Appl Sci Eng. 2021;13(1):42–6. [CrossRef].
24. Nkrumah I, Ampong FK, Britwum A, Paal M, Kwakye-Awuah B, Nkum RK, et al. Determining the majority charge carrier, optical and structural properties of electrochemically deposited lead tin sulfide (PbSnS) thin films. Chalcogenide Lett. 2023;20(3):205–13. [CrossRef].
25. Li CP, Asom MT, McNeil LE. Strain relaxation in PbSnSe and PbSe epilayers grown on BaF_2 (111) substrates. J Cryst Growth. 2000;209(1):206–12. [CrossRef].
26. Sist M, Zhang J, Brummerstedt Iversen B. Crystal structure and phase transition of thermoelectric SnSe. Acta Crystallogr B Struct Sci Cryst Eng Mater. 2016;72(Pt 3):310–6. [CrossRef].
27. Im HS, Myung Y, Cho YJ, Kim CH, Kim HS, Back SH, et al. Facile phase and composition tuned synthesis of tin chalcogenide nanocrystals. RSC Adv. 2013;3(26):10349. [CrossRef].

28. Midgett AG, Luther JM, Stewart JT, Smith DK, Padilha LA, Klimov VI, et al. Size and composition dependent multiple exciton generation efficiency in PbS, PbSe, and PbS_xSe_{1-x} alloyed quantum dots. Nano Lett. 2013;13(7):3078–85. [CrossRef].
29. Deb AK, Kumar V. Bandgap engineering in semiconducting one to few layers of SnS and SnSe. Phys Status Solidi B. 2017;254(2):1600379. [CrossRef].
30. Koteeswara Reddy N, Devika M, Gopal ESR. Review on tin (II) sulfide (SnS) material: synthesis, properties, and applications. Crit Rev Solid State Mater Sci. 2015;40(6):359–98. [CrossRef].
31. Kang I, Wise FW. Electronic structure and optical properties of PbS and PbSe quantum dots. J Opt Soc Am B. 1997;14(7):1632. [CrossRef].
32. Tripathy SK, Pattanaik A. Optical and electronic properties of some semiconductors from energy gaps. Opt Mater. 2016;53:123–33. [CrossRef].
33. Rhee JH, Chung CC, Diau EW. A perspective of mesoscopic solar cells based on metal chalcogenide quantum dots and organometal-halide perovskites. NPG Asia Mater. 2013;5(10):e68. [CrossRef].
34. Zhang J, Gao J, Miller EM, Luther JM, Beard MC. Diffusion-controlled synthesis of PbS and PbSe quantum dots with *in situ* halide passivation for quantum dot solar cells. ACS Nano. 2014;8(1):614–22. [CrossRef].
35. Wise FW. Lead salt quantum dots: the limit of strong quantum confinement. Acc Chem Res. 2000;33(11):773–80. [CrossRef].
36. Dong C, Liu S, Barange N, Lee J, Pardue T, Yi X, et al. Long-wavelength lead sulfide quantum dots sensing up to 2600 nm for short-wavelength infrared photodetectors. ACS Appl Mater Interfaces. 2019;11(47):44451–7. [CrossRef].
37. Moreels I, Lambert K, Smeets D, De Muynck D, Nollet T, Martins JC, et al. Size-dependent optical properties of colloidal PbS quantum dots. ACS Nano. 2009;3(10):3023–30. [CrossRef].
38. He Z, Liu H, Xie F, Bai M, Wen S, Zhao J, et al. Lead selenium colloidal quantum dots for 400-2600 nm broadband photodetectors. J Nanomater. 2022;2022:2940382. [CrossRef].
39. Chen M, Hao Q. Colloidal Quantum Dots for Nanophotonic Devices. Materials. 2024;17(11):2471.[CrossRef].
40. Lee H, Park WJ, Wang J, Heo J. Optical properties of Pb1–Sn Se quantum dots (QDs) in silicate glasses dictated by GeO_2 concentrations. J Non Cryst Solids. 2018;482:177–82. [CrossRef].
41. Liu C, Heo J. Band gap and diameter modulation of quantum dots in glasses. Int J Appl Glass Sci. 2015;6(4):329–38. [CrossRef].
42. Han Y, Fang X, Shi Z. Advances in chalcogenide perovskites: fundamentals and applications. Appl Phys Rev. 2024;11(2):021338. [CrossRef].
43. Ren S, Wang M, Wang X, Han G, Zhang Y, Zhao H, et al. Near-infrared heavy-metal-free SnSe/ZnSe quantum dots for efficient photoelectrochemical hydrogen generation. Nanoscale. 2021;13(6):3519–27. [CrossRef].